

PAPER • OPEN ACCESS

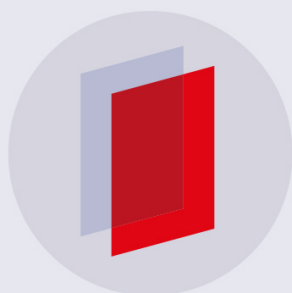
Intrinsic electronic transport and thermoelectric power factor in n-type doped monolayer MoS₂

To cite this article: Yinchang Zhao *et al* 2018 *New J. Phys.* **20** 043009

View the [article online](#) for updates and enhancements.

Related content

- [Potential 2D thermoelectric material ATel \(A = Sb and Bi\) monolayers from a first-principles study](#)
San-Dong Guo, Ai-Xia Zhang and Hui-Chao Li
- [Thermoelectric properties of SnSe₂ monolayer](#)
Guanpeng Li, Guangqian Ding and Guoying Gao
- [First-principles calculations of thermal, electrical, and thermoelectric transport properties of semiconductors](#)
Jiawei Zhou, Bolin Liao and Gang Chen



IOP | ebooksTM

Bringing you innovative digital publishing with leading voices to create your essential collection of books in STEM research.

Start exploring the collection - download the first chapter of every title for free.



PAPER

Intrinsic electronic transport and thermoelectric power factor in n -type doped monolayer MoS_2

OPEN ACCESS

RECEIVED

30 December 2017

REVISED

8 February 2018

ACCEPTED FOR PUBLICATION

1 March 2018

PUBLISHED

12 April 2018

Original content from this work may be used under the terms of the [Creative Commons Attribution 3.0 licence](#).

Any further distribution of this work must maintain attribution to the author(s) and the title of the work, journal citation and DOI.



Yinchang Zhao^{1,5}, Zhenhong Dai^{1,5} , Chao Zhang¹ , Chao Lian², Shuming Zeng³, Geng Li³, Sheng Meng^{2,4,5} and Jun Ni^{3,4,5}

¹ Department of Physics, Yantai University, Yantai 264005, People's Republic of China

² Beijing National Laboratory for Condensed Matter Physics and Institute of Physics, Chinese Academy of Sciences, Beijing, 100190, People's Republic of China

³ State Key Laboratory of Low-Dimensional Quantum Physics, Department of Physics, Tsinghua University, Beijing 100084, People's Republic of China

⁴ Collaborative Innovation Center of Quantum Matter, Beijing 100084, People's Republic of China

⁵ Authors to whom any correspondence should be addressed.

E-mail: y.zhao@ytu.edu.cn, zhdai@ytu.edu.cn, smeng@iphy.ac.cn and junni@mail.tsinghua.edu.cn

Keywords: electron–phonon coupling, electronic transport, Boltzmann transport equation, thermoelectric power factor, thermal conductivity, mobility

Abstract

The electronic transport and thermoelectric properties in n -type doped monolayer MoS_2 are investigated by a parameter-free method based on first-principles calculations, electron–phonon coupling (EPC), and Boltzmann transport equation (BTE). Remarkably, the calculated electron mobility $\mu \sim 47 \text{ cm}^2 \text{ V}^{-1} \text{ s}^{-1}$ and thermoelectric power factor $\sigma S^2 \sim 2.93 \times 10^{-3} \text{ W m}^{-1} \text{ K}^{-2}$ at room temperature are much lower than the previous theoretical values (e.g. $\mu \sim 130\text{--}410 \text{ cm}^2 \text{ V}^{-1} \text{ s}^{-1}$ and $\sigma S^2 \sim 2.80 \times 10^{-2} \text{ W m}^{-1} \text{ K}^{-2}$), but agree well with the most recent experimental findings of $\mu \sim 37 \text{ cm}^2 \text{ V}^{-1} \text{ s}^{-1}$ and $\sigma S^2 \sim 3.00 \times 10^{-3} \text{ W m}^{-1} \text{ K}^{-2}$. The EPC projections on phonon dispersion and the phonon branch dependent scattering rates indicate that the acoustic phonons, especially the longitudinal acoustic phonons, dominate the carrier scattering. Therefore, a mobility of $68 \text{ cm}^2 \text{ V}^{-1} \text{ s}^{-1}$ is achieved if only the acoustic phonons induced scattering is included, in accordance with the result of $72 \text{ cm}^2 \text{ V}^{-1} \text{ s}^{-1}$ estimated from the deformation potential driven by acoustic modes. Furthermore, via excluding the scattering from the out-of-plane modes to simulate the EPC suppression, the obtained mobility of $258 \text{ cm}^2 \text{ V}^{-1} \text{ s}^{-1}$ is right in the range of $200\text{--}700 \text{ cm}^2 \text{ V}^{-1} \text{ s}^{-1}$ measured in the samples with top deposited dielectric layer. In addition, we also compute the lattice thermal conductivity κ_L of monolayer MoS_2 using phonon BTE, and obtain a $\kappa_L \sim 123 \text{ W m}^{-1} \text{ K}^{-1}$ at 300 K.

1. Introduction

As a prototypical transition metal dichalcogenide, molybdenum disulfide (MoS_2) has drawn a great deal of attention owing to its excellent electronic and optical properties [1–4]. Similar to graphite, bulk MoS_2 is comprised of stacked layers that are loosely coupled by Van der Waals interaction [5]. This weak interlayer interaction makes fabrication of monolayer MoS_2 be probable by micromechanical exfoliation from the bulk counterpart [5–7], same as the synthesis of graphene from graphite [8]. While bulk MoS_2 is an indirect band-gap semiconductor with the gap of about 1.2 eV [9], monolayer MoS_2 has a direct band gap $\sim 1.9 \text{ eV}$ [5, 6], which is right in the range of visible frequency, and consequently promise the applications such as photodetector, transistors [7], and electroluminescent devices. In addition, due to the strong electron–phonon coupling (EPC), monolayer MoS_2 also exhibits good conventional superconductivity when the sample is heavily n -type doped [10–13].

In recent years, studies on electronic transport and thermoelectric properties of monolayer MoS_2 have gained increased interest because characterization of transport properties, especially the intrinsic transport, is

crucial to assess and understand its potential significance. For a suspended monolayer MoS₂, the electron mobility μ is found early to be in the range of 0.5–3 cm² V⁻¹ s⁻¹ [8]. Much higher mobilities of 200–700 cm² V⁻¹ s⁻¹ can be reached through high- κ gate dielectric engineering to effectively screen the charged-impurities scattering and suppress the electron–phonon scattering [7, 14–16]. Theoretically, the phonon-mediated intrinsic mobilities have been calculated to be 130–410 cm² V⁻¹ s⁻¹ at room temperature according to the full band Monte Carlo simulations, EPC matrix calculations, or the deformation potential couplings in combination of Fröhlich interactions [17–20]. However, the deformation potential theory based on only the acoustic phonon scattering mechanism indicates that monolayer MoS₂ possesses an electron mobility of 72 cm² V⁻¹ s⁻¹ [21]. In view of further decrease of the mobility by inclusion of optical phonon scattering, this result is in sharp contrast to the theoretical values above 130 cm² V⁻¹ s⁻¹ [17–20]. Moreover, a most recent experimental measure on monolayer MoS₂ shows a small electron mobility of only 37 cm² V⁻¹ s⁻¹ at room temperature [22], and a prior Hall measurement exhibits a mobility of only 64 cm² V⁻¹ s⁻¹ at 260 K [23]. Besides the electron mobility, the measured thermoelectric power factor $\sigma S^2 \sim 3.00 \times 10^{-3}$ W m⁻¹ K⁻² [22] is also much lower than previous computational results such as 2.80×10^{-2} W m⁻¹ K⁻² [24]. Therefore, to solve these discrepancies, it is important to reestimate the electron mobility and power factor of monolayer MoS₂ with refined calculations.

In this work, we investigate the electronic and thermoelectric transport of *n*-type doped monolayer MoS₂ by a parameter-free first-principles technique. The calculated mobility $\mu \sim 47$ cm² V⁻¹ s⁻¹ and power factor $\sigma S^2 \sim 2.93 \times 10^{-3}$ W m⁻¹ K⁻² at 300 K show good agreement with the most recent experimental findings [22]. With the scattering induced by only the acoustic phonons, the obtained mobility of 68 cm² V⁻¹ s⁻¹ accords with the result of 72 cm² V⁻¹ s⁻¹ estimated from the acoustic phonon-mediated deformation potential [21]. Via excluding the scattering from the out-of-plane vibrations to simulate the EPC suppression, the estimated mobility of 258 cm² V⁻¹ s⁻¹ is comparable to the experimental results measured in the samples with top deposited dielectric layer. The calculated lattice thermal conductivity $\kappa_L \sim 123$ W m⁻¹ K⁻¹ at 300 K is also consistent with the previous calculations.

2. Methodology

Our electronic and thermoelectric transport properties of *n*-type doped monolayer MoS₂ are calculated from the electron Boltzmann transport equation (BTE) and the first-principles density functional theory as implemented in the QUANTUM-ESPRESSO package [25]. The norm-conserving pseudopotential is used to model the ion cores, and a plane-wave basis set with the cutoff energy of 80 Ry and the exchange-correlation functional of local-density approximation (LDA) with Perdew–Zunger parametrization [26] is chosen to simulate the valance electrons. A vacuum space of 15 Å is taken to eliminate the interactions between MoS₂ layer and its periodic images. To calculate the phonon dispersion and EPC matrix, the density functional perturbation theory and the Wannier interpolation technique are applied [27]. The electronic structure and dynamical matrix are both initially calculated within a $36 \times 36 \times 1$ grid, and then uniformly interpolated into a dense mesh of $216 \times 216 \times 1$ by using the maximally localized Wannier functions as coded in the EPW package [28, 29]. With the interpolated dense EPC matrix elements, the *k*-dependent electron lifetime can be obtained, which is taken as the input quantity for the electron BTE.

From the electron Boltzmann theory, we can write the electrical conductivity σ and thermopower S along the α axis as follows [30, 31]

$$\sigma_{\alpha\alpha} = -\frac{e^2}{N_k \Omega} \sum_{nk} (v_{nk}^\alpha)^2 \tau_{nk}^{\text{el}} \frac{\partial f_{nk}}{\partial \varepsilon_{nk}}, \quad (1)$$

$$S_{\alpha\alpha} = -\frac{1}{eT} \frac{\sum_{nk} (\varepsilon_{nk} - \varepsilon_F) (v_{nk}^\alpha)^2 \tau_{nk}^{\text{el}} \frac{\partial f_{nk}}{\partial \varepsilon_{nk}}}{\sum_{nk} (v_{nk}^\alpha)^2 \tau_{nk}^{\text{el}} \frac{\partial f_{nk}}{\partial \varepsilon_{nk}}}, \quad (2)$$

where N_k , Ω , T , and ε_F are the total number of *k* points in the full Brillouin zone (BZ), volume of the unit cell, absolute temperature, and Fermi energy, respectively. ε_{nk} is the energy eigenvalue of Khon–Sham state $|nk\rangle$, f_{nk} is Fermi–Dirac distribution function of $|nk\rangle$, and v_{nk}^α is the corresponding electron group velocity along the α axis. τ_{nk}^{el} is the electron lifetime calculated according to the relationship

$$\tau_{nk}^{\text{el}} = \frac{\hbar}{2\Sigma''_{nk}}, \quad (3)$$

where Σ''_{nk} is the imaginary part of electron self-energy, also known as electron linewidth. Σ''_{nk} is calculated from the EPC by the formula [29]

$$\begin{aligned} \Sigma''_{nk} = & \pi \sum_{m\nu} \int_{\text{BZ}} \frac{d\mathbf{q}}{\Omega_{\text{BZ}}} |g_{mm,\nu}(\mathbf{k}, \mathbf{q})|^2 \times [(n_{q\nu} + f_{m\mathbf{k}+\mathbf{q}})\delta(\varepsilon_{n\mathbf{k}} - \varepsilon_{m\mathbf{k}+\mathbf{q}} - \hbar\omega_{q\nu}) \\ & + (n_{q\nu} + 1 - f_{m\mathbf{k}+\mathbf{q}})\delta(\varepsilon_{n\mathbf{k}} - \varepsilon_{m\mathbf{k}+\mathbf{q}} + \hbar\omega_{q\nu})], \end{aligned} \quad (4)$$

where Ω_{BZ} is the volume of the full BZ, $\omega_{q\nu}$ and $n_{q\nu}$ are the phonon frequency and equilibrium Bose–Einstein distribution function of phonon mode $|\mathbf{q}\nu\rangle$, and

$$g_{mm,\nu}(\mathbf{k}, \mathbf{q}) = \sqrt{\frac{\hbar}{2M\omega_{q\nu}}} \langle m\mathbf{k} + \mathbf{q} | \partial_{\mathbf{q}\nu} V | n\mathbf{k} \rangle \quad (5)$$

is the EPC matrix element induced by mode $|\mathbf{q}\nu\rangle$ between states $|m\mathbf{k} + \mathbf{q}\rangle$ and $|n\mathbf{k}\rangle$. In equation (5), M is the atomic mass, $\partial_{\mathbf{q}\nu} V$ is the derivative of the Kohn–Sham potential with respect to atomic displacement associated with the phonon mode $|\mathbf{q}\nu\rangle$. Following the calculation of electrical conductivity σ , the mobility μ is obtained by

$$\mu = \frac{1}{e} \frac{d\sigma}{dn}, \quad (6)$$

where n is the doping concentration computed from the integral of electron density of states (EDOS) by

$$n = \frac{e}{N_k \Omega} \sum_{nk} [f_{nk}(\varepsilon_F, T) - f_{nk}(\varepsilon_{F0}, T)] \quad (7)$$

with ε_{F0} as the Fermi energy of the undoped sample.

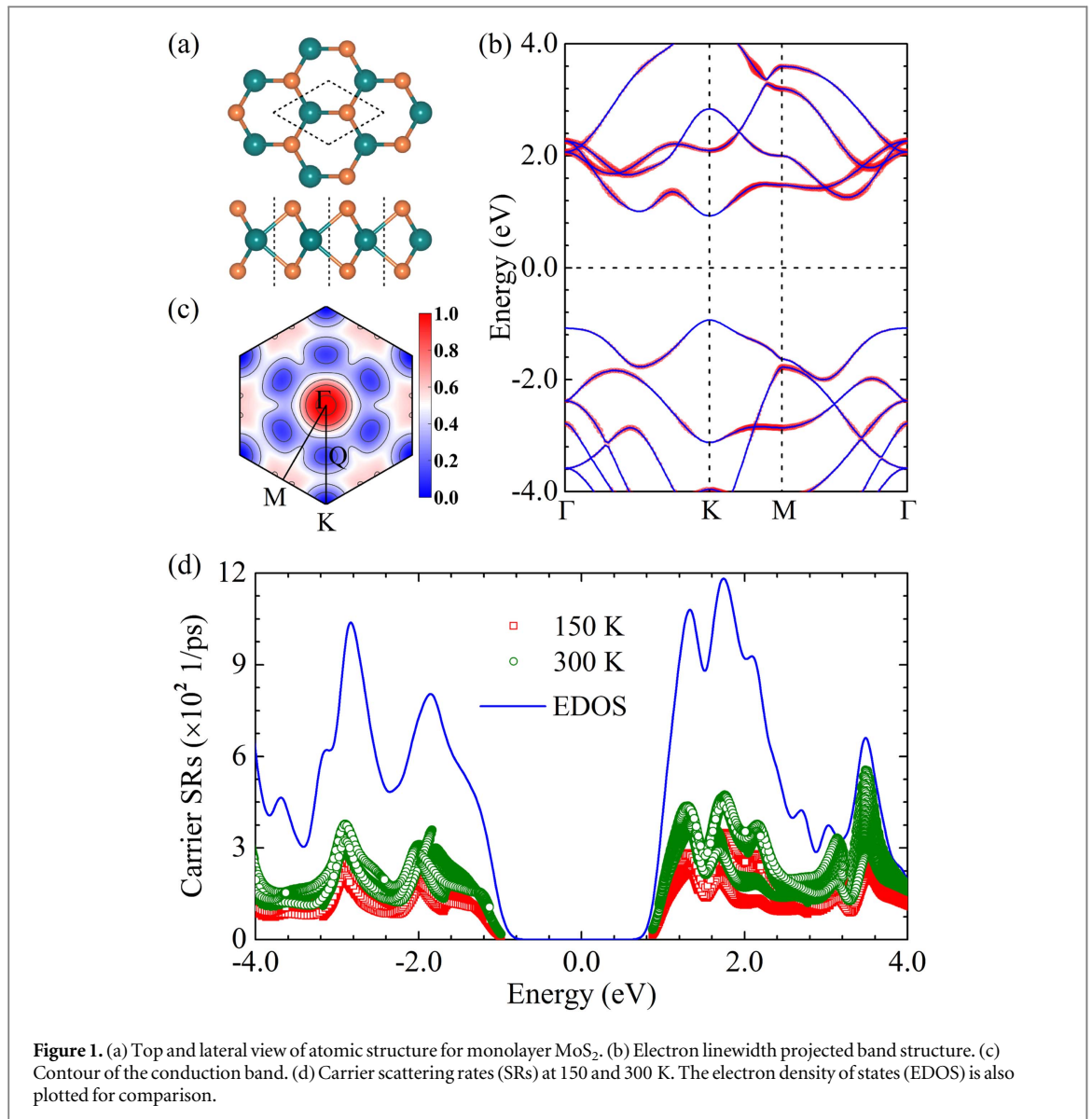
The lattice thermal conductivity κ_L is obtained by solving the phonon BTE [32], where the anharmonic interatomic force constants (IFCs) are generated within $5 \times 5 \times 1$ supercells by the finite-difference approach. The interaction up to fifth-nearest neighbors is included in the calculations of anharmonic IFCs, and a q -mesh of $40 \times 40 \times 1$ is used to ensure the convergence of κ_L .

3. Results and discussion

The energetically stable monolayer MoS₂ is the $2H$ phase with the symmetry D_{3h} , in which a molybdenum (Mo) layer is sandwiched between two sulfur (S) layers, as sketched in figure 1(a). Since the largest effective thermoelectric power factor σS^2 is captured around a small electron doping concentration $n \sim 6.0 \times 10^{12} \text{ cm}^{-2}$ (corresponding to about $0.005e$ per unit cell) [22] and the band structure and phonon dispersion have almost no change induced by such weak doping [13, 19], the rigid band model of the undoped monolayer MoS₂ is sufficient to study the EPC and carrier scattering rates (SRs). Hence, unless otherwise stated, we take the undoped $2H$ phase and the rigid band model to study the transport properties of n -type doped monolayer MoS₂ in this paper. The doping concentration n at temperature T is calculated according to equation (7) by shifting Fermi level ε_F .

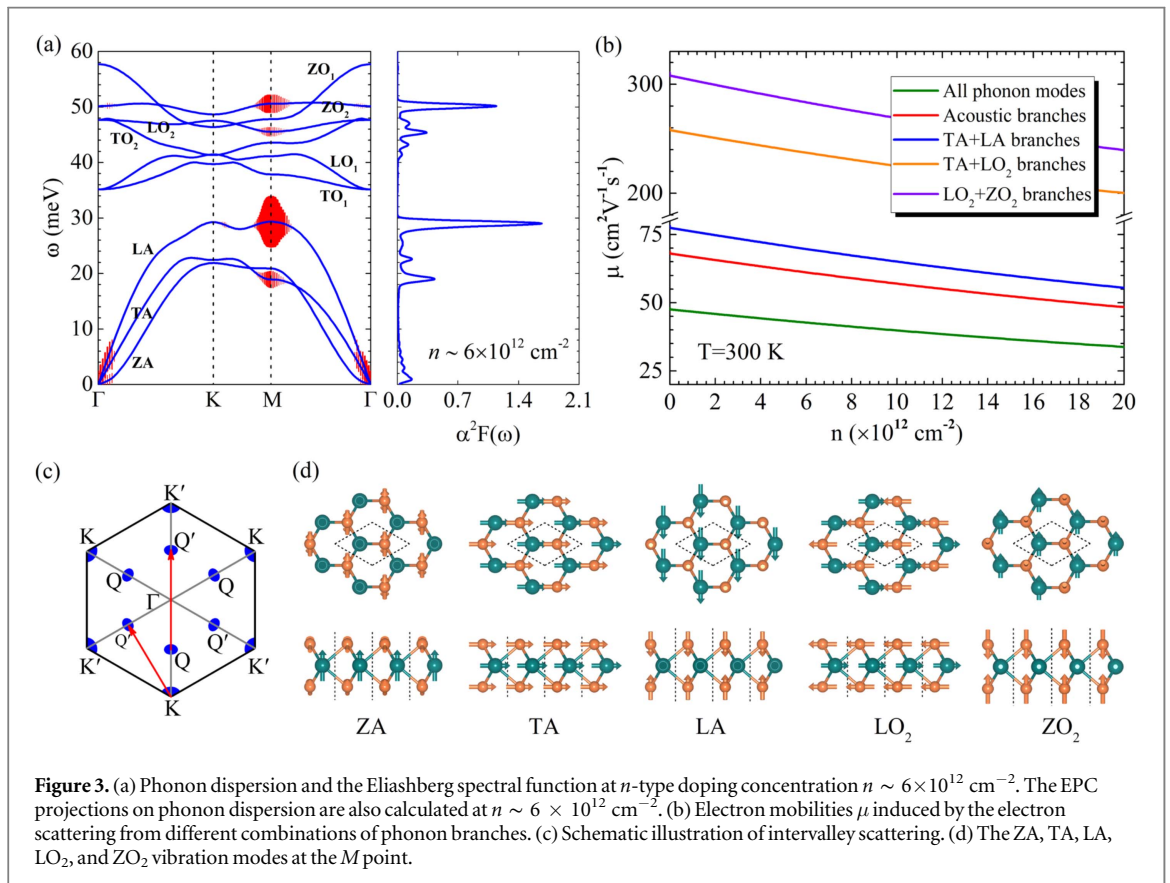
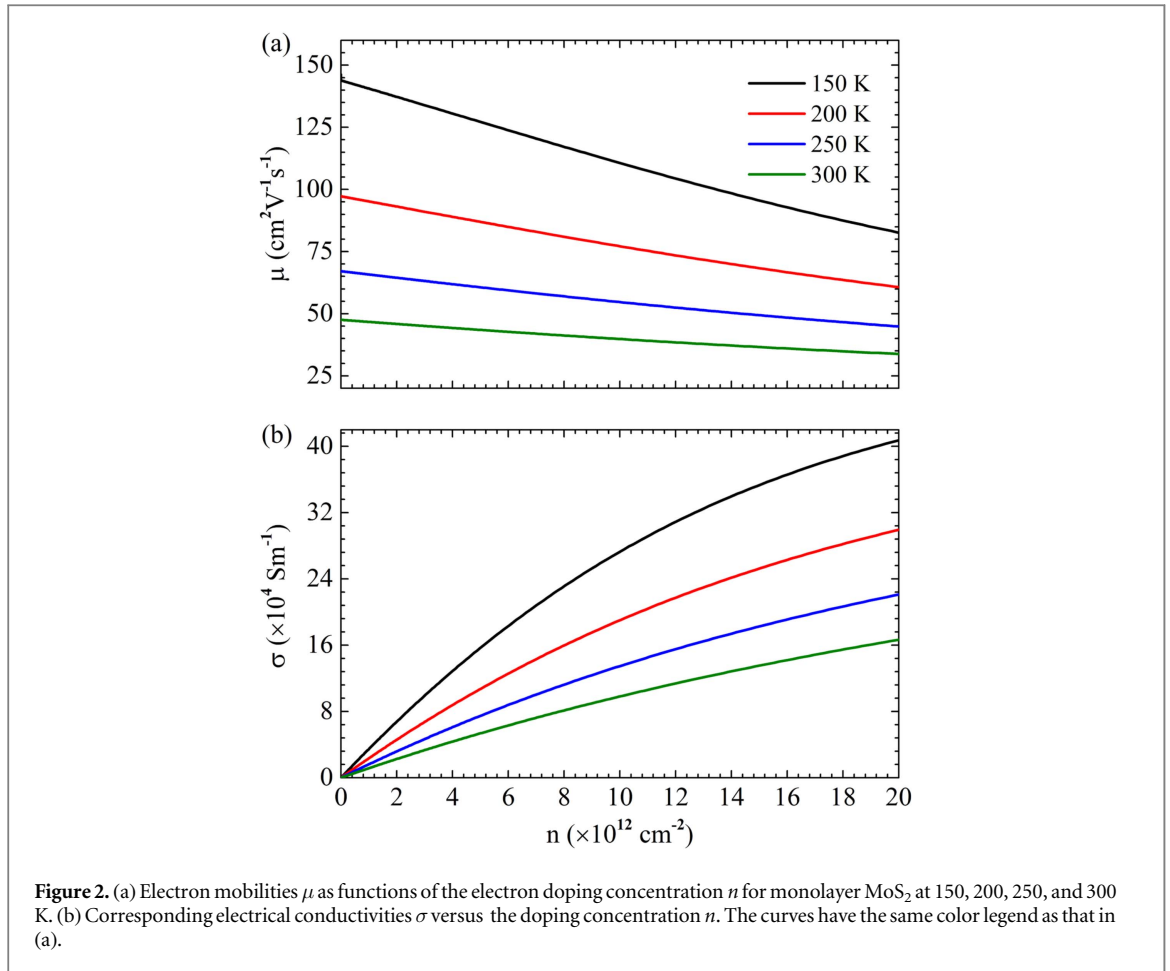
The optimized lattice constant, thickness, and Mo–S bond length are 3.14, 3.12, and 2.39 Å, respectively, which are in accordance with other reported results [13, 33–35]. The calculated band structure predicts a direct band gap of 1.86 eV between the valence band maximum (VBM) and conduction band minimum (CBM) at the K point in the BZ, as shown in figure 1(b). For the conduction band, we also detect the existence of the second energy minima (the so-called Q valley), which is about 82 meV higher than the CBM and locates approximately at the halfway point of the ΓK line, as shown in figures 1(b) and (c). The band dispersion around the energy minima in the conduction band is almost quadratic and thus can be described by the effective mass approximation. The calculated longitudinal and transverse effective masses for the Q valley are $m_Q^l = 0.61m_e$ and $m_Q^t = 0.99m_e$, respectively, with the longitudinal direction fixed along the ΓK axis and m_e denoting the free electron mass, while the K valley (CBM at the K point) shows a nearly isotropic effective mass of $0.49m_e$. These characters of band structure are consistent with those in the previous works [5, 6, 10, 13, 18, 36, 37]. The electron linewidth, which is an indicator of the carrier scattering, is also projected on the band structure. It exhibits that there is relatively small linewidth and thus weak scattering around the VBM and the Q and K valleys. To illustrate total scattering, the carrier SRs in the whole BZ as a function of energy at 150 and 300 K are shown in figure 1(d). Overall, raising the temperature T increases the carrier SRs almost uniformly. The SRs at the same T follow closely the EDOS since the accessible phase space reflects the magnitude of the EDOS. The small SRs at the band edges correspond to the small linewidth projections around the VBM and the Q and K valleys, which leads to a largest electron lifetime of e.g. 30.7 fs for the conduction bands at 300 K.

The calculated electron mobilities μ and electrical conductivities σ as functions of the doping concentration n for the n -type doped monolayer MoS₂ at 150–300 K are plotted in figure 2. The conductivity σ is re-scaled according to equation (1) by a factor of c/h , where c is the vacuum space of 15 Å and h is the effective thickness ~ 6.5 Å of the monolayer MoS₂ sheet [38]. As shown in figure 2, both the mobility μ and conductivity σ decrease with the increasing T at the same n , consistent with the change of SRs versus T . At the same T , in contrast to the decrease of mobility μ versus n , the conductivity σ increases with n due to the enhancement of EDOS. At room



temperature, the calculated maximum value of the electron mobility is $\mu \sim 47 \text{ cm}^2 \text{ V}^{-1} \text{ s}^{-1}$, which is much lower than the theoretical values of $130\text{--}410 \text{ cm}^2 \text{ V}^{-1} \text{ s}^{-1}$ [17–20]. Compared with the experimental data, this result is in agreement with the most recent finding of $37 \text{ cm}^2 \text{ V}^{-1} \text{ s}^{-1}$ [22], although it is much higher than the early data in the range of $0.5\text{--}3 \text{ cm}^2 \text{ V}^{-1} \text{ s}^{-1}$ [8] and much lower than the values of $200\text{--}700 \text{ cm}^2 \text{ V}^{-1} \text{ s}^{-1}$ [7, 14–16]. It is worth noting that the experimental data of $200\text{--}700 \text{ cm}^2 \text{ V}^{-1} \text{ s}^{-1}$ are achieved by top deposited high- κ gate dielectric engineering, in which the electron–phonon scattering in the interlayer MoS₂ sheet would be effectively screened by the top deposited dielectric layers and substrate, and thus results in high mobilities [7, 14–16]. However, the recent finding of $37 \text{ cm}^2 \text{ V}^{-1} \text{ s}^{-1}$ is measured in a perfect monolayer MoS₂ on the SiO₂ substrate [22], which lacks of the screening of electron–phonon scattering from the top deposited dielectric layers, and gives rise to a mobility much more close to the intrinsic one. Considering the reduction of mobility resulted from the screenings of electron–phonon scattering from the SiO₂ substrate in [22], our calculated intrinsic value of $\mu \sim 47 \text{ cm}^2 \text{ V}^{-1} \text{ s}^{-1}$ agrees well with the finding of $37 \text{ cm}^2 \text{ V}^{-1} \text{ s}^{-1}$. In addition, the analyses in the experimental works in [39, 40] have revealed that the coupling capacitance between top and bottom gates is ignored in the mobility measurements based on the two-point method in the thin-film MoS₂ transistor channel, which results in an overestimation of the mobility by a factor of about 14. With this effect in consideration, the modified data from the experiments show the mobility values being much smaller than the theoretical predictions of $130\text{--}410 \text{ cm}^2 \text{ V}^{-1} \text{ s}^{-1}$. A subsequent Hall measurement also exhibited a small mobility of about $64 \text{ cm}^2 \text{ V}^{-1} \text{ s}^{-1}$ at 260 K [23], with which our result of $\mu \sim 68 \text{ cm}^2 \text{ V}^{-1} \text{ s}^{-1}$ at 250 K shows good agreement, as shown in figure 2(a).

To reveal the internal electronic transport mechanism, the phonon dispersion, Eliashberg spectral function, and intervalley scattering schematic are shown in figures 3(a) and (c). For phonon dispersion, there are three



acoustic branches: out-of-plane acoustic (ZA), transverse acoustic (TA), and longitudinal acoustic (LA) branches, which are separated by a gap of about 5.73 meV below the nonpolar transverse optical (TO₁) and longitudinal optical (LO₁) modes. The TO₂, LO₂, and ZO₁ modes represent three polar optical branches, while the ZO₂ branch is homopolar with a nondispersive behavior and a breathing mode eigenvector. The Eliashberg spectral function

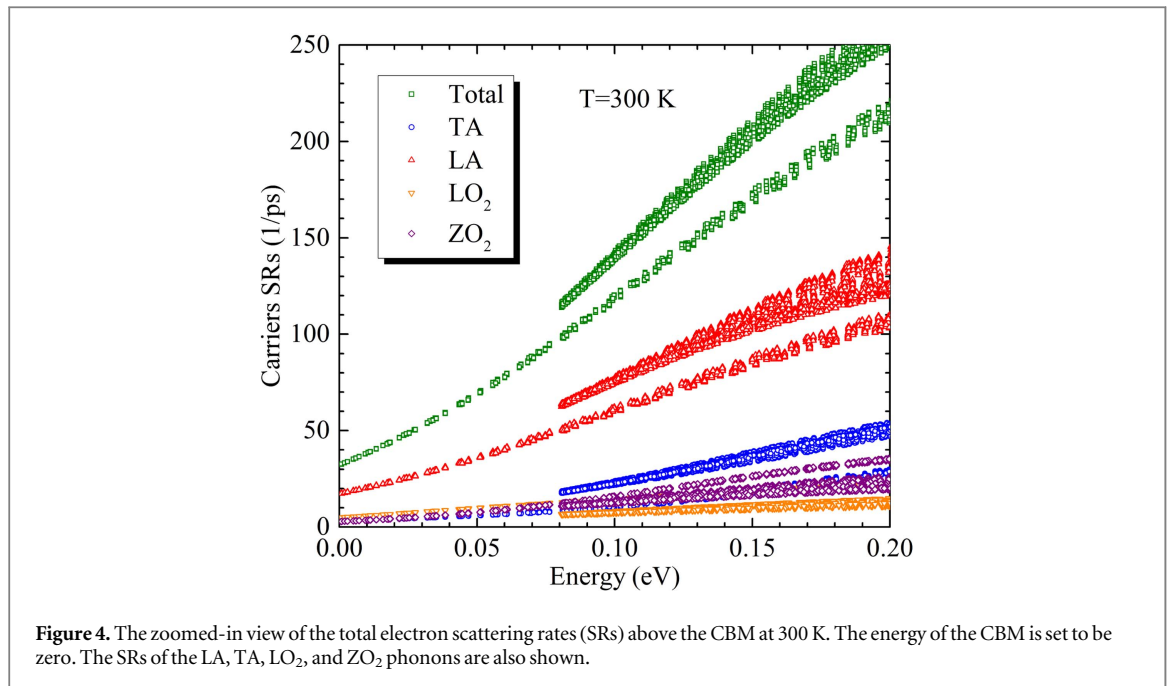
$$\alpha^2 F(\omega) = \frac{1}{2N(\varepsilon_F)\omega_{q\nu}} \sum_{mm,\nu} \int_{\text{BZ}} \frac{d\mathbf{q}}{\Omega_{\text{BZ}}} \int_{\text{BZ}} \frac{d\mathbf{k}}{\Omega_{\text{BZ}}} |g_{mm,\nu}(\mathbf{k}, \mathbf{q})|^2 \omega_{q\nu} \times \delta(\varepsilon_{n\mathbf{k}} - \varepsilon_F) \delta(\varepsilon_{m\mathbf{k}+\mathbf{q}} - \varepsilon_F) \delta(\omega - \omega_{q\nu}), \quad (8)$$

which represents the density of EPC strength in phonon frequency space, is calculated at the n -type doping concentration $n \sim 6.0 \times 10^{12} \text{ cm}^{-2}$, at which the largest effective thermoelectric power factor σS^2 is experimentally captured [22]. The EPC projections on phonon dispersion are also computed at this doping concentration. Evidently, the peaks in Eliashberg spectral function $\alpha^2 F(\omega)$ corresponds to the EPC projections on phonon dispersion. These results indicate that the TA, LA, LO₂, and ZO₂ phonons around the M point give rise to the main EPC and thus govern the electron scattering, as shown in figure 3(a). This is due to the fact that the phonons around the M point can induce electron intervalley scattering between the K and Q' valleys, as sketched in figure 3(c). In addition, around the Γ point, due to small phonon wave vector, the presence of intravalley scattering results in some EPC projections on the ZO₂ and three acoustic branches; near the K point, the electron transition from the Q to Q' valleys will lead to the projections on the TA and LA branches.

In contrast to optical phonons dominating the electron scattering [17], our results show that the acoustic modes, especially the LA and TA phonons around the M point, play significant roles in the scattering, as shown in figure 3(a), which is consistent with the analysis in [18–20]. Via including the electron scattering induced by only the acoustic phonons, our calculated mobility is $\mu \sim 68 \text{ cm}^2 \text{ V}^{-1} \text{ s}^{-1}$, as shown in figure 3(b), which accords well with the value of $72 \text{ cm}^2 \text{ V}^{-1} \text{ s}^{-1}$ estimated from the acoustic phonon-mediated deformation potential [21]. In fact, the EPC strength captured in the acoustic phonon-mediated deformation potential also originate mainly from the LA and TA phonons [21], because the ZA modes are relatively insensitive to the tiny deformation. If the electron scattering from only the LA and TA phonons is taken into account, the obtained mobility is $\mu \sim 76 \text{ cm}^2 \text{ V}^{-1} \text{ s}^{-1}$, as shown in figure 3(b), which also shows a good agreement with the result of $72 \text{ cm}^2 \text{ V}^{-1} \text{ s}^{-1}$ in [21]. In addition, the electronic transport caused by only the optical modes is also computed to mimic the result without inclusion of the scattering from the acoustic modes in [17]. Among the six optical branches, only the LO₂ and ZO₂ modes induce considerable EPC, as shown in figure 3(a). If only the electron-phonon scattering arising from the LO₂ and ZO₂ modes is considered, the obtained mobility is $\mu \sim 310 \text{ cm}^2 \text{ V}^{-1} \text{ s}^{-1}$, as shown in figure 3(b), which is comparable to the result of $410 \text{ cm}^2 \text{ V}^{-1} \text{ s}^{-1}$ in [17].

The experimental works that exhibit the mobilities of 200–700 $\text{cm}^2 \text{ V}^{-1} \text{ s}^{-1}$ at room temperature are achieved by top deposited high- κ gate dielectric engineering [7, 14–16]. In these experiments, monolayer MoS₂ is the interlayer of the sandwich structure and its charged-impurities scattering and the electron-phonon scattering would be effectively screened by the substrate and dielectric layers. Before estimating the mobility of this monolayer MoS₂, we firstly show the vibration modes of the three acoustic and the LO₂ and ZO₂ optical branches at the M point in figure 3(d). Evidently, the vibrations along the out-of-plane direction, such as ZA, LA, ZO₂ modes at the M point, for the MoS₂ interlayer in the sandwich structure are easily quenched by top deposited dielectric layer and substrate. As a result, only the in-plane vibration modes induced EPC dominates the electron scattering. As shown in figures 3(a) and (d), the in-plane vibration modes resulting in strong EPC are only the TA and LO₂ phonons around the M point. With the scattering driven by only the TA and LO₂ phonons, we obtain a mobility $\mu \sim 258 \text{ cm}^2 \text{ V}^{-1} \text{ s}^{-1}$ at 300 K, which is just in the range of 200–700 $\text{cm}^2 \text{ V}^{-1} \text{ s}^{-1}$ [7, 14–16]. Although the method of excluding the EPC contributions from the out-of-plane phonon modes is not very accurate to simulate the EPC suppression quantitatively, our results indicate that the mobility can be sharply enhanced once the out-of-plane modes are quelled by top deposition and substrate.

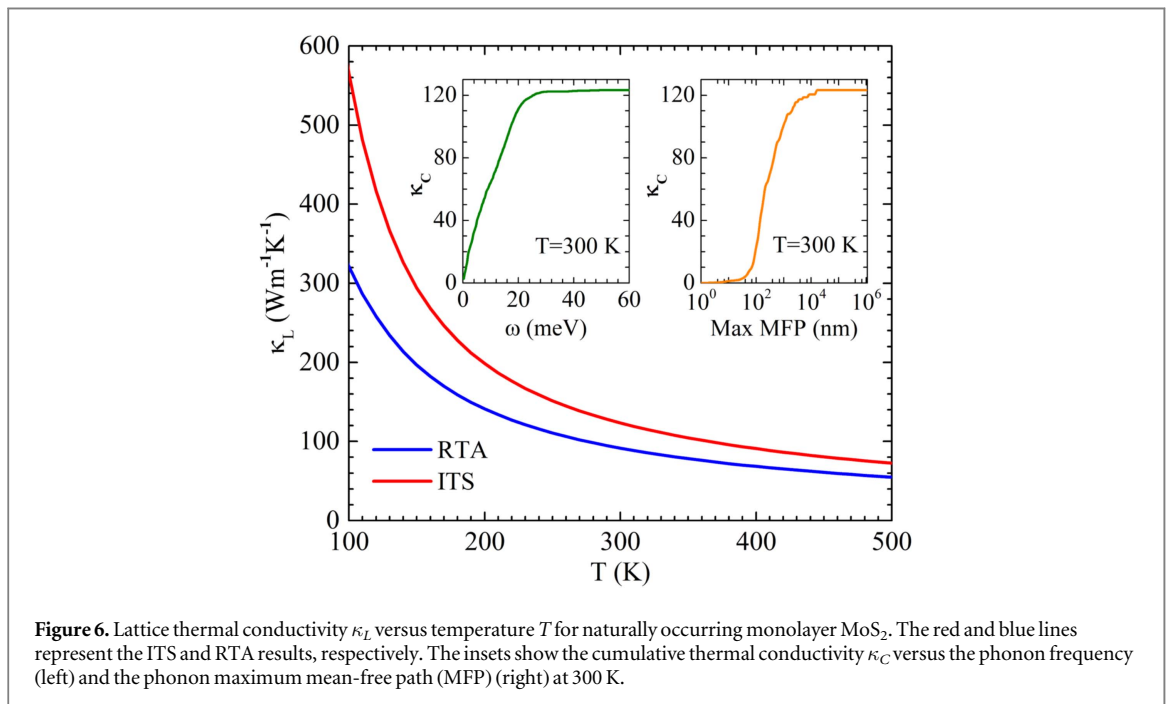
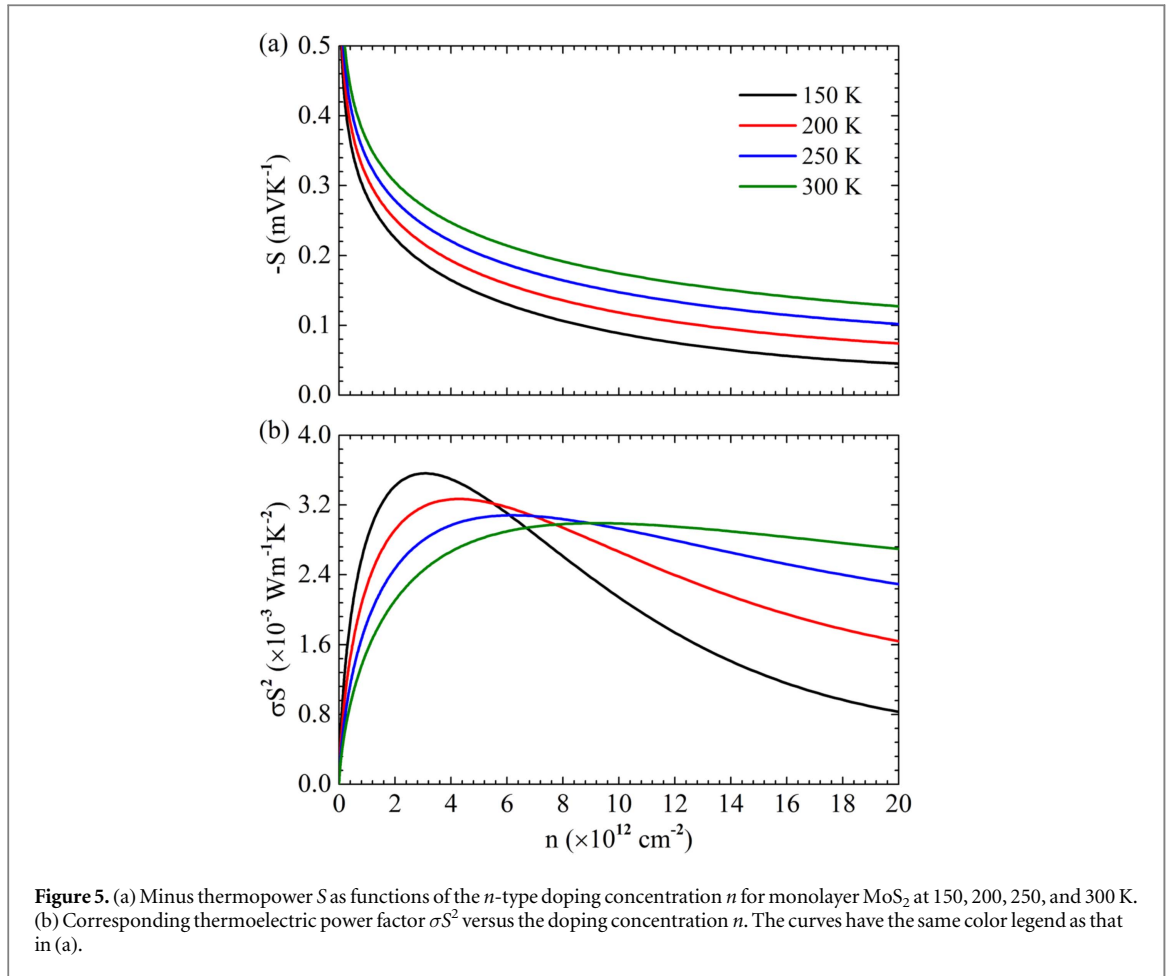
In order to clarify the discrepancies between our mobilities and the results of 130 and 150 $\text{cm}^2 \text{ V}^{-1} \text{ s}^{-1}$ obtained by the similar method to ours [18, 20], we show the zoomed-in view of the total electron SRs near the CBM in figure 4. The SRs originating from the LA, TA, LO₂, and ZO₂ phonons are also shown in figure 4 (for the electron SRs of each phonon branch, see figure A1 in appendix). Obviously, the LA phonons contribute the main SRs of the monolayer MoS₂, being consistent with the EPC projections in figure 3(a). At 82 meV above the CBM, which is just the energy of the so-called Q and Q' valleys, the electron scattering between Q and Q' valleys gets involved, which, as a result, leads to an additional distribution for the total electron SRs and the SRs of each phonon branch. This is not distinguished clearly in figure 3(a), because the carrier concentration $n \sim 6.0 \times 10^{12} \text{ cm}^{-2}$ used in the EPC projection calculations corresponds to the electron doping of only about 20 meV above the CBM. For the EPC projections at heavy doping, see figure 3(a) in [13]. Strikingly, around the CBM, the calculated carrier SRs are about three times higher than those in the previous calculations (see figures 7 and 8 in [20]). It is based on these higher carrier SRs of monolayer MoS₂ that our calculated mobilities of



47 cm² V⁻¹ s⁻¹ at 300 K and 68 cm² V⁻¹ s⁻¹ at 250 K are in good agreement with the most recent experimental finding of 37 cm² V⁻¹ s⁻¹ at 300 K [22] and the prior Hall measurement result of 64 cm² V⁻¹ s⁻¹ at 260 K [23]. Moreover, as analyzed above, the electron mobility estimated from the acoustic phonon-mediated deformation potential in [21], the mobility induced by only the optical phonons in [17], and a high mobility comparable to the values measured in the samples with top deposited dielectric layer in [7, 14–16] can be rightly simulated based on these higher carrier SRs through excluding part of electron–phonon scattering according to their respective physical mechanisms. These results support that our calculated carrier SRs are more rational than those in the previous works [18, 20]. It is worth noting that our carrier SRs are obtained from the relationship $1/\tau_{nk}^{el} = 2\Sigma_{nk}''/\hbar$, where the electron linewidth Σ_{nk}'' is outputted directly by the EPW package [28, 29], while the specific computational process of the linewidth Σ_{nk}'' in [20] is unknown. To test the validity of our predictions for carrier SRs, we also calculate the electron SRs of crystalline Si, as shown in figure A2 in appendix. The calculated SRs of Si at 300 K is identical to the result in the EPW examples (see figure 8 in [29]), indicating the validity of our computing method.

The calculated thermopower S and thermoelectric power factor σS^2 for the n -type doped monolayer MoS₂ at 150–300 K are plotted in figure 5. Owing to the minus value of S in monolayer MoS₂ with the n -type doping, the $-S$ is plotted for convenience. As shown in figure 5(a), the $-S$ increases with temperature T at the same doping concentration n , and decreases with n at the same T , similar to the tendency observed in majority of semiconducting thermoelectric materials. The values of the calculated $-S$ are fairly large, although they are smaller than previous computational results [24]. For instance, our calculations give the $-S$ of about 0.37 mV K⁻¹ at $T = 300$ K and $n \sim 10^{12}$ cm⁻² while a value of 0.52 mV K⁻¹ is obtained at the same conditions in [24]. Obviously, both of the two values exceed the range of 0.20–0.30 mV K⁻¹ which is the typical thermopower for a good thermoelectric material. As shown in figure 5(b), the largest power factor σS^2 at each temperature has a value exceeding 2.93×10^{-3} W m⁻¹ K⁻², which is comparable to that of Bi₂Te₃. At 300 K, the largest power factor $\sigma S^2 \sim 2.93 \times 10^{-3}$ W m⁻¹ K⁻² can be achieved at $n \sim 10^{13}$ cm⁻², and a power factor of about 2.80×10^{-3} W m⁻¹ K⁻² is obtained at $n \sim 6.0 \times 10^{12}$ cm⁻². These power factor values show good agreement with the most recent experimental finding of $\sigma S^2 \sim 3.00 \times 10^{-3}$ W m⁻¹ K⁻² around $n \sim 6.0 \times 10^{12}$ cm⁻² [22], although they are about one order of magnitude smaller than the result of 2.80×10^{-2} W m⁻¹ K⁻² in [24].

The high power factor hints a good thermoelectric performance if the thermal conductivity is lower enough. For monolayer MoS₂, the lattice thermal conductivity is reported to be in the range of 18–140 W m⁻¹ K⁻¹ at room temperature when an effective thickness of 6.5 Å is used [41–44]. Here we calculate the lattice thermal conductivity κ_L of the monolayer MoS₂ by solving the phonon BTE with the harmonic and anharmonic IFCs as input quantities, which has been demonstrated to be an accurate and predictive method for studying the thermal transport performance [45–49]. The calculated κ_L of the naturally occurring sample as a function of T is plotted in figure 6. Similar to the conductivity σ , the κ_L is also re-scaled by the factor of c/h , where the effective thickness h is set to be 6.5 Å. The iterative solutions (ITS) of the phonon BTE and the relaxation time approximation (RTA) results are both shown, which indicates a difference smaller than 30% for the κ_L above 300 K. At 300 K,



the ITS (RTA) results of the κ_L is about 123 (92) $\text{W m}^{-1} \text{ K}^{-1}$, just in the range of 18–140 $\text{W m}^{-1} \text{ K}^{-1}$ [41–44]. This relatively high κ_L combined with the high power factor σS^2 indicates that two-dimensional monolayer MoS_2 is not suitable for design of thermoelectric generator (figure of merit $ZT < 0.01$ at 300 K), but holds promise for in-plane thin-film Peltier coolers, in which a high power factor and a high thermal conductivity are both required [24]. In addition, the κ_L of the doped MoS_2 would be modified if more scattering processes are

included. It is reported that the EPC plays important role in lattice thermal transport in heavy doping samples. For instance, the lattice thermal conductivity of crystalline Si may reduce 45% at a heavy p -type doping of about 10^{21} cm^{-3} [50, 51]. The four-phonon scattering also has a significant influence on lattice thermal transport, e.g. four-phonon scattering reduces the intrinsic thermal conductivity of graphene and decreases the contributions from flexural phonons [52]. The calculated κ_L of the n -type doped MoS₂ sheet may be reduced significantly if these effects are included, and thus the figure of merit ZT would also be modified.

In addition, we have also investigated the cumulative thermal conductivity κ_C with respect to the allowed phonon frequency and phonon maximum mean-free path (MFP), respectively, as shown by the insets in figure 6. The κ_C versus the phonon frequency gives the summed contribution from all phonon modes below the specified frequency, which exhibits that almost all of the κ_L ($\sim 99\%$) is dominated by the acoustic phonon modes. The κ_C versus the phonon maximum MFP reveals the size dependence of the κ_L , which indicates that the phonons with a MFP shorter than 100 nm dominate about 20% of the total κ_L , implying the nanostructures with a characteristic length of the phonon MFP smaller than 100 nm are required to reduce the κ_L drastically. Furthermore, if the nanostructures with the MFP characteristic length shorter than 10 nm is applied, the κ_L may be reduced to $1.20 \text{ W m}^{-1} \text{ K}^{-1}$, and thus a figure of merit $ZT \sim 0.73$ can be obtained at 300 K.

4. Conclusion

In summary, we have used a parameter-free method based on first-principles technique, EPC, and BTE to investigate the electronic transport and thermoelectric properties in n -type doped monolayer MoS₂. Due to the higher carrier scattering rates (SRs) than those of the previous calculations, our calculated electron mobilities μ of $47 \text{ cm}^2 \text{ V}^{-1} \text{ s}^{-1}$ at 300 K and $68 \text{ cm}^2 \text{ V}^{-1} \text{ s}^{-1}$ at 250 K show good agreement with the experimental findings of $37 \text{ cm}^2 \text{ V}^{-1} \text{ s}^{-1}$ at 300 K and $64 \text{ cm}^2 \text{ V}^{-1} \text{ s}^{-1}$ at 260 K. The EPC projections on phonon dispersion and the phonon branch dependent SRs indicate that the acoustic phonons, especially the longitudinal acoustic phonons, dominate the carrier scattering. Thus, the obtained acoustic phonon induced mobility is only about $68 \text{ cm}^2 \text{ V}^{-1} \text{ s}^{-1}$, which accords well with the result of $72 \text{ cm}^2 \text{ V}^{-1} \text{ s}^{-1}$ estimated from the deformation potential driven by acoustic modes. Meanwhile, the mobility $\mu \sim 310 \text{ cm}^2 \text{ V}^{-1} \text{ s}^{-1}$ induced by only the optical modes is close to the value of $410 \text{ cm}^2 \text{ V}^{-1} \text{ s}^{-1}$ without inclusion of the scattering from the acoustic phonons. Furthermore, via excluding the scattering from the out-of-plane modes to simulate the EPC suppression, the calculated mobility $\mu \sim 258 \text{ cm}^2 \text{ V}^{-1} \text{ s}^{-1}$ is right in the range of $200\text{--}700 \text{ cm}^2 \text{ V}^{-1} \text{ s}^{-1}$ measured in the samples with top deposited dielectric layer. Due to the rationality of the electronic transport properties, our calculated thermoelectric power factor $\sigma S^2 \sim 2.93 \times 10^{-3} \text{ W m}^{-1} \text{ K}^{-2}$ is also consistent with the experimental value of $\sigma S^2 \sim 3.00 \times 10^{-3} \text{ W m}^{-1} \text{ K}^{-2}$. In addition, the computed lattice thermal conductivity $\kappa_L \sim 123 \text{ W m}^{-1} \text{ K}^{-1}$ at 300 K by the phonon BTE also shows consistency with the previous works. These results clarify the discrepancies between the experimental results and previous theoretical values, and shed further light on the electronic and thermoelectric transport of monolayer MoS₂.

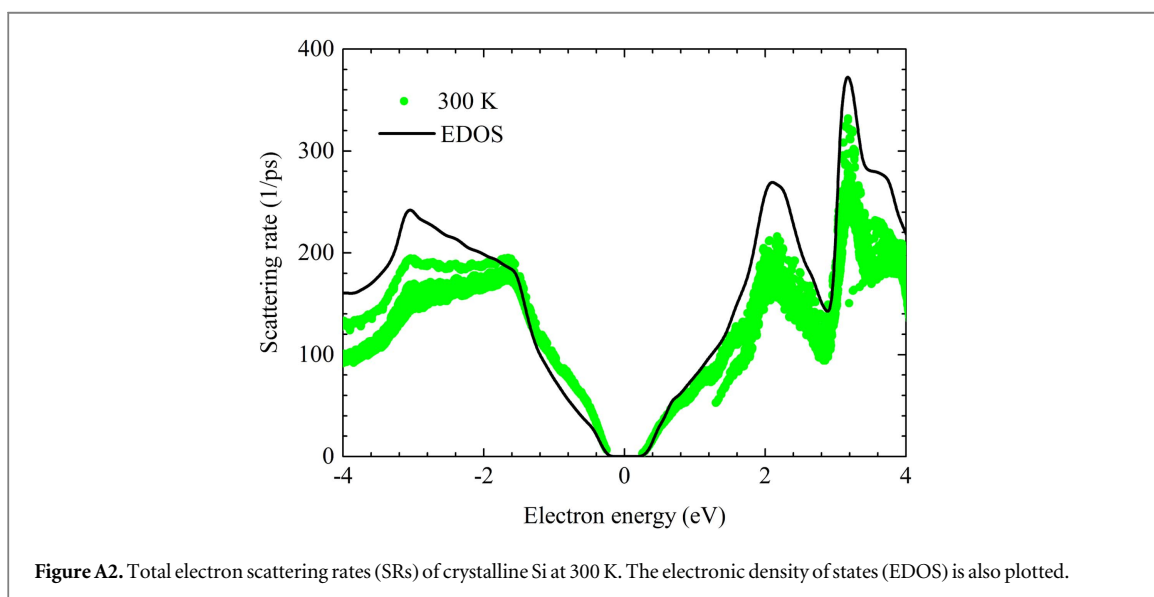
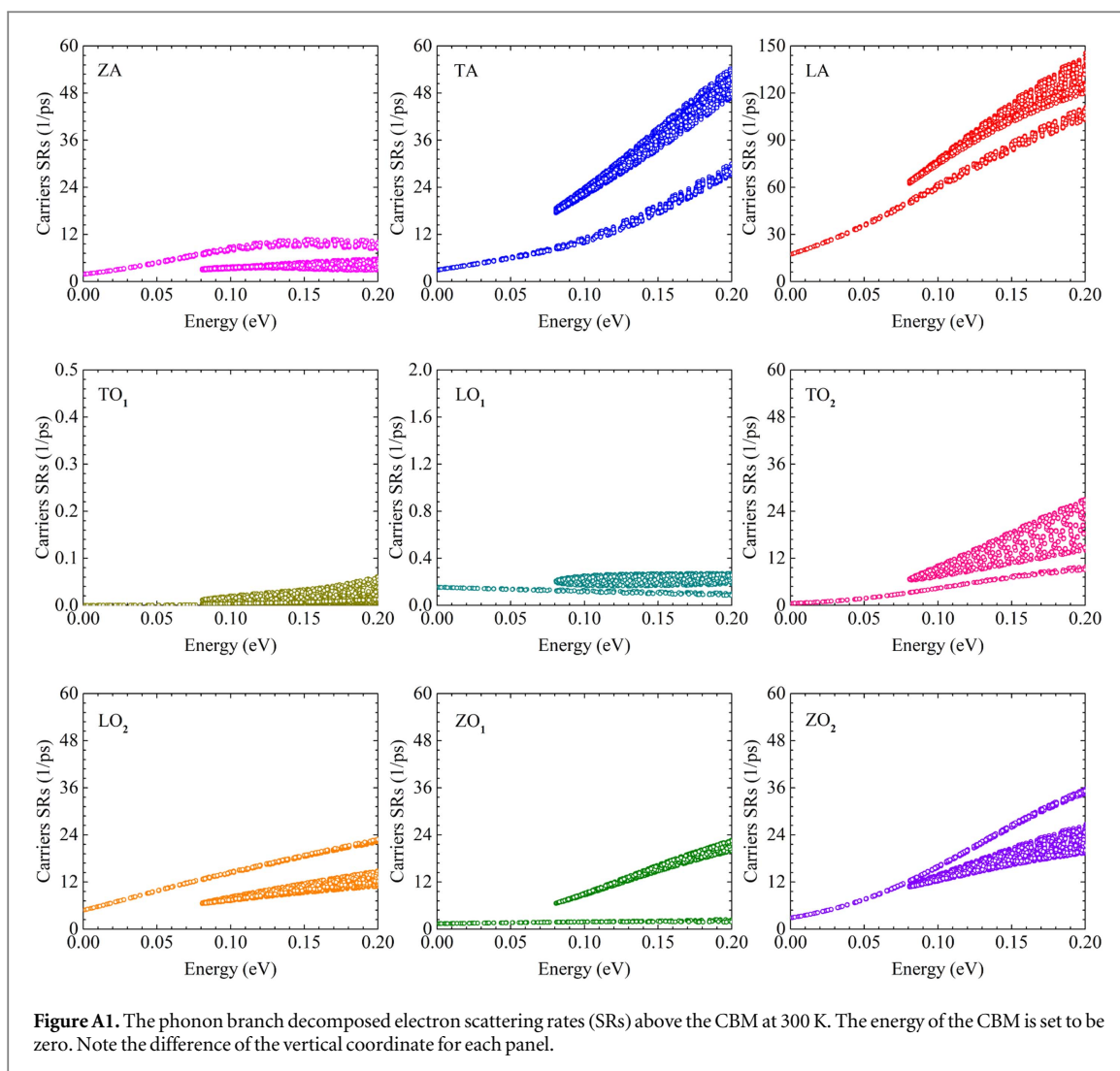
Acknowledgments

This research was supported by the National Natural Science Foundation of China under Grants Nos. 11704322, 11774396, and 11774195, the National Key Research and Development Program of China under Grants Nos. 2016YFA0300902 and 2016YFB0700102, the MOST Project of China under Grants No. 2015CB921001, and the Natural Science Foundation of Shandong Province for Doctoral Program under Grant No. ZR2017BA017.

Appendix

The electron SRs arising from nine phonon branches are shown in figure A1. Note the difference of the vertical coordinate for each panel. Above 82 meV, due to the presence of the scattering between Q and Q' valleys, there is an additional distribution for the SRs of each phonon branch. It can be clearly found that the LA phonons contribute the main electron SRs. At low doping (below 82 meV), besides the LA phonons, the ZA, TA, LO₂, and ZO₂ phonons also play important roles in the SRs, as shown in figure A1.

To test the validity of our predictions for carrier SRs, we calculate the electron SRs of crystalline Si. The norm-conserving pseudopotential and a plane-wave basis set with the cutoff energy of 65 Ry and the LDA exchange-correlation functional are used. The electronic structure and dynamical matrix are both initially calculated within a $10 \times 10 \times 10$ grid, and then uniformly interpolated into a dense mesh of $40 \times 40 \times 40$. The calculated total electron SRs at 300 K is shown in figure A2. The EDOS is also plotted for comparison. The



calculated EDOS and SRs of Si at 300 K are identical to the results in the EPW examples (see figure 8 in [29]), which indicates the validity of our computing method.

ORCID iDs

Zhenhong Dai  <https://orcid.org/0000-0002-8559-3196>

Chao Zhang  <https://orcid.org/0000-0002-5957-2287>

References

- [1] Wang Q H, Kalantar-Zadeh K, Kis A, Coleman J N and Strano M S 2012 *Nat. Nanotechnol.* **7** 699
- [2] Feng J, Qian X, Huang C-W and Li J 2012 *Nat. Photon.* **6** 866
- [3] Conley H J, Wang B, Ziegler J I, Haglund R F, Pantelides S T and Bolotin K I 2013 *Nano Lett.* **13** 3626
- [4] Castellanos-Gomez A, Roldán R, Cappelluti E, Buscema M, Guinea F, van der Zant H S J and Steele G A 2013 *Nano Lett.* **13** 5361
- [5] Mak K F, Lee C, Hone J, Shan J and Heinz T F 2010 *Phys. Rev. Lett.* **105** 136805
- [6] Splendiani A, Sun L, Zhang Y, Li T, Kim J, Chim C-Y, Galli G and Wang F 2010 *Nano Lett.* **10** 1271
- [7] Radisavljevic B, Radenovic A, Brivio J, Giacometti I V and Kis A 2011 *Nat. Nanotechnol.* **6** 147
- [8] Novoselov K, Jiang D, Schedin F, Booth T, Khotkevich V, Morozov S and Geim A 2005 *Proc. Natl. Acad. Sci. USA* **102** 10451
- [9] Kam K K and Parkinson B A 1982 *J. Phys. Chem.* **86** 463
- [10] Ge Y and Liu A Y 2013 *Phys. Rev. B* **87** 241408
- [11] Das T and Dolui K 2015 *Phys. Rev. B* **91** 094510
- [12] Huang G Q, Xing Z W and Xing D Y 2016 *Phys. Rev. B* **93** 104511
- [13] Zeng S, Zhao Y, Li G and Ni J 2016 *Phys. Rev. B* **94** 024501
- [14] Wang H, Yu L, Lee Y-H, Shi Y, Hsu A, Chin M L, Li L-J, Dubey M, Kong J and Palacios T 2012 *Nano Lett.* **12** 4674
- [15] Bao W, Cai X, Kim D, Sridhara K and Fuhrer M S 2013 *Appl. Phys. Lett.* **102** 042104
- [16] Das S, Chen H-Y, Penumatcha A V and Appenzeller J 2013 *Nano Lett.* **13** 100
- [17] Kaasbjerg K, Thygesen K S and Jacobsen K W 2012 *Phys. Rev. B* **85** 115317
- [18] Li X, Mullen J T, Jin Z, Borysenko K M, Buongiorno Nardelli M and Kim K W 2013 *Phys. Rev. B* **87** 115418
- [19] Ge Y, Wan W, Feng W, Xiao D and Yao Y 2014 *Phys. Rev. B* **90** 035414
- [20] Li W 2015 *Phys. Rev. B* **92** 075405
- [21] Cai Y, Zhang G and Zhang Y-W 2014 *J. Am. Chem. Soc.* **136** 6269
- [22] Hippalgaonkar K, Wang Y, Ye Y, Qiu D Y, Zhu H, Wang Y, Moore J, Louie S G and Zhang X 2017 *Phys. Rev. B* **95** 115407
- [23] Radisavljevic B and Kis A 2013 *Nat. Mater.* **12** 815
- [24] Babaei H, Khodadadi J M and Sinha S 2014 *Appl. Phys. Lett.* **105** 193901
- [25] Giannozzi P et al 2009 *J. Phys.: Condens. Matter* **21** 395502
- [26] Perdew J P and Zunger A 1981 *Phys. Rev. B* **23** 5048
- [27] Giustino F, Cohen M L and Louie S G 2007 *Phys. Rev. B* **76** 165108
- [28] Noffsinger J, Giustino F, Malone B D, Park C-H, Louie S G and Cohen M L 2010 *Comput. Phys. Commun.* **181** 2140
- [29] Poncé S, Margine E, Verdi C and Giustino F 2016 *Comput. Phys. Commun.* **209** 116
- [30] Liao B, Zhou J, Qiu B, Dresselhaus M S and Chen G 2015 *Phys. Rev. B* **91** 235419
- [31] Zhao Y, Dai Z, Lian C, Zeng S, Li G, Ni J and Meng S 2017 *Phys. Rev. Mater.* **1** 065401
- [32] Li W, Carrete J, Katcho N A and Mingo N 2014 *Comput. Phys. Commun.* **185** 1747
- [33] Chang C-H, Fan X, Lin S-H and Kuo J-L 2013 *Phys. Rev. B* **88** 195420
- [34] Ataca C, Topsakal M, Aktürk E and Ciraci S 2011 *J. Phys. Chem. C* **115** 16354
- [35] Huang L F, Gong P L and Zeng Z 2014 *Phys. Rev. B* **90** 045409
- [36] Ellis J K, Lucero M J and Scuseria G E 2011 *Appl. Phys. Lett.* **99** 261908
- [37] Molina-Sánchez A, Palumbo M, Marini A and Wirtz L 2016 *Phys. Rev. B* **93** 155435
- [38] Frindt R F 1966 *J. Appl. Phys.* **37** 1928
- [39] Fuhrer M S and Hone J 2013 *Nat. Nanotechnol.* **8** 146
- [40] Radisavljevic B and Kis A 2013 *Nat. Nanotechnol.* **8** 147
- [41] Yan R, Simpson J R, Bertolazzi S, Brivio J, Watson M, Wu X, Kis A, Luo T, Hight Walker A R and Xing H G 2014 *ACS Nano* **8** 986
- [42] Sahoo S, Gaur A P S, Ahmadi M, Guinel M J-F and Katiyar R S 2013 *J. Phys. Chem. C* **117** 9042
- [43] Wu X, Yang N and Luo T 2015 *Appl. Phys. Lett.* **107** 191907
- [44] Gu X and Yang R 2014 *Appl. Phys. Lett.* **105** 131903
- [45] Dekura H, Tsuchiya T and Tsuchiya J 2013 *Phys. Rev. Lett.* **110** 025904
- [46] Zhao Y, Dai Z, Zhang C, Lian C, Zeng S, Li G, Meng S and Ni J 2017 *Phys. Rev. B* **95** 014307
- [47] Pang J W L, Buyers W J L, Chernatynskiy A, Lumsden M D, Larson B C and Phillpot S R 2013 *Phys. Rev. Lett.* **110** 157401
- [48] Zhao Y, Dai Z, Lian C and Meng S 2017 *RSC Adv.* **7** 25803
- [49] Lindsay L, Broido D A and Reinecke T L 2013 *Phys. Rev. Lett.* **111** 025901
- [50] Liao B, Maznev A A, Nelson K A and Chen G 2016 *Nat. Commun.* **7** 13174
- [51] Liao B, Qiu B, Zhou J, Huberman S, Esfarjani K and Chen G 2015 *Phys. Rev. Lett.* **114** 115901
- [52] Feng T and Ruan X 2018 *Phys. Rev. B* **97** 045202